Quenching of a heated wall with spatial temperature gradient using a liquid film through oblique jet impingement

Noritaka Sako[1*], Kouhei Noda[1], Jun Hayashi[1], Yu Daimon[2] and Hiroshi Kawanabe[1]

[1] Department of Energy Science, Kyoto University, Yoshida Honmachi, Sakyo-ku, Kyoto 606-8501, Japan

E-mail : sako.noritaka.32c@st.kyoto-u.ac.jp

[2] Research Unit III, Research and Development Directorate, Japan Aerospace Exploration Agency, 2-1-1 Sengen, Tsukuba, Ibaraki 305-8505, Japan

Abstract

The quenching of a heated aluminum alloy plate with a spatial temperature gradient by water jet impingement was experimentally investigated to examine the effect of the liquid mass flow rate and liquid jet velocity by varying the nozzle diameter. The behavior of the liquid film formed by jet impingement was observed by high-speed imaging, and the temperature profile of the test plate was measured by infrared imaging. In addition, the surface heat flux and the amount of the heat removal, from the test plate to the liquid film, were calculated by inverse heat conduction analysis to investigate the heat transfer characteristics between the liquid film and test plate and to estimate the mass fraction of the injected liquid contributing to cooling. Results indicated that the wetting front propagation was affected by the mass flow rate, rather than by the liquid jet velocity. From the estimated results obtained by inverse heat conduction analysis, it was found that the values of the maximum heat flux, whose position lay near the wetting front, were almost the same under the same mass flow rate condition even though the liquid jet velocity was about 2.5 times different. In addition, from the estimation of the amount of heat removal, it was found that about 90 % of the injected liquid was splashed away from the test plate without evaporation.

Key Words: quenching, oblique jet impingement, liquid film, wetting front

Nomenclature

a	constant value defined by Eq. (1) [dimensional number depending on n]
c_{w}	specific heat of the test plate [J kg^{-1} K^{-1}]
d	inner diameter of nozzle [m]
h_{lv}	latent heat of the test liquid [J kg^{-1}]
H	liquid film thickness [m]
k_{w}	thermal conductivity of the test plate [W m^{-1} K^{-1}]
$\dot{m}$	mass flow rate [kg s^{-1}]
n	exponent value defined by Eq. (1) [-]
Pe	Peclet number [-]
q_{max}	maximum heat flux [W m^{-2}]
q_{s}	surface heat flux [W m^{-2}]
$\dot{Q}$	amount of heat removal from the plate to the liquid film [W]
Re_{j}	jet Reynolds number ($=\frac{u_{\mathrm{j}}d}{\nu}$) [-]
t	elapsed time after the liquid injection [s]
T_{w}	temperature of the test plate [K]
ΔT_{sub}	degree of subcooling [K]
ΔT_{sup}	degree of wall superheat [K]
u_{j}	jet velocity at the nozzle exit [m s^{-1}]
u_{wf}	velocity of the wetting front [m s^{-1}]
x_{wf}	position of the wetting front relative to the impingement point [m]
x, y, and z	coordinates of the impingement point of the liquid jet [m]
α_{w}	thermal diffusivity of the test plate [m^2 s^{-1}]
δ	thickness of the wall [m]
θ	impingement angle [°]

ν kinematic viscosity of the test liquid [m^2 s^{-1}]

ρ_l density of the test liquid [kg m^{-3}]

ρ_w density of the test plate [kg m^{-3}]

$\emptyset$ evaporative rate defined by Eq. (4) [-]

1. Introduction

Impinging jet cooling, as a liquid film, is widely employed in industrial fields, for example, in material processes [1, 2, 3] and cooling of nuclear reactor cores [4, 5]. Bipropellant thrusters for orbit maneuvering and attitude control of satellites also employ the film-cooling technique using liquid jets of the fuel impinging onto the chamber wall [6, 7]. In bipropellant thrusters, nitrogen tetroxide/hydrazine-derivative fuel (for example, hydrazine, monomethylhydrazine, and unsymmetrical dimethylhydrazine) propellants, which react immediately upon coming into contact even at low pressures and temperatures [8, 9, 10], are generally preferred. Owing to their unique and fast reactivity, bipropellant propulsion systems are operated using pulse-mode firing with the firing time ranging O (10–10^2) ms [6, 11]. During the combustion, the highest wall temperature appears around the throat part, and a large temperature gradient was formed from the throat to the impingement point [12]. If the interval between each firing pulse is too short to allow for the sufficient cooling of the chamber wall, the fuel for film cooling is injected onto the hot wall with a spatial temperature gradient. This spatial temperature gradient is formed by the heat stored particularly around the throat at the previous combustion. The stored heat is transferred towards the injector side by the thermal diffusion. This is known as heat soak-back [13]. Figure 1 shows a schematic of the process of the situation mentioned above.

It is known that most of the liquid splashes away from the leading edge of the liquid film because of the vapor flow induced by vigorous boiling when the liquid jet is injected onto a hot surface whose temperature exceeds the saturated temperature or the Leidenfrost temperature of the liquid [14, 15]. Recently, Fu et al. [16] conducted a Computational Fluid Dynamics (CFD) analysis of a bipropellant rocket engine with a droplet/wall impact model incorporating five modes. The five modes are (1) stick/spread, (2) boiling with breakup, (3) suspend, (4) rebound, and (5) splash, depending on the conditions of the droplet Weber number and surface temperature. These results suggest that film splashing may occur under the operating conditions of the thruster, as shown in Fig. 1. The quenching processes should be investigated to predict the liquid film behavior concerning hazard prevention and the shortening of the liquid film length with respect to the steady-state combustion mode.

Investigations on vertical jet impingement quenching of hot surfaces in steel and nuclear industries and on the liquid film behavior and the heat transfer characteristic between the liquid film and hot surface have been extensively conducted. As mentioned above, during quenching of the hot surface by the impinging jet, a large amount of liquid is deflected away from the surface at the leading edge of the liquid film, and different cooling modes, such as forced convection, nucleate boiling, transient boiling, and film boiling coexist on the surface, which makes it difficult to understand the cooling processes [14, 15]. The boundary between the wetted region and the dry region is called as the wetting front (WF) [17, 18]. The position of the maximum heat flux, essential for understanding the quenching phenomena, was located within the wetted region rather than at the WF [1, 3, 19]. The WF moves downstream with the passage of time, and the velocity of the WF and the value of the maximum heat flux decrease with the radial position of the WF [15, 18, 20].

The position of WF has often been correlated with the power function of the elapsed time, as shown in Eq. (1).

$$x_{\mathrm{wf}} = a \cdot t^{n}, \tag{1}$$

where x_{wf} is the distance from the impingement point of the liquid jet to the position of the WF. The WF radius was found to increase in proportion to the square root of time (n = 0.5) [20]. Mitsutake and Monde [18] investigated the effects of the liquid jet velocity u_{j}, liquid subcooling, and thermal properties of the test blocks on the constant a and exponent n, and it was observed that the constant a increased linearly with liquid jet velocity and liquid subcooling and assumed a higher value for a smaller value of the thermal inertia of the test blocks. The exponent, n, was observed to be independent of the liquid jet velocity and the thermal property of the block, and weakly affected by the liquid subcooling. Karwa et al. [15] remarked that there were two possible reasons for the decrease of the WF velocity. One of the reasons was the deceleration of the liquid film that relates to its ability to detach the bubbles from the surface. The other reason was that the liquid was more superheated as the distance traveled by the liquid increases with the expanding WF position, leading to a reduction in the ability to condense the bubbles at the WF. However, the physical model for the WF behavior has not still been elucidated [21], primarily owing to the poor understanding of the physical processes during the transient cooling [22].

Although there were several parameters affecting the film formation processes such as the momentum flow rate per unit length [23] and the impingement angle [7, 24, 25], experimental results for the behavior of the WF and surface heat flux were discussed and organized, mainly focusing on the velocity of the liquid jet that was related to the velocity of the liquid film [1, 18, 19]. On the other hand, it was recently reported that the hydrodynamics of the WF and the heat transfer characteristics were determined by the flow rate of the test liquid [26]. This suggests that the WF behavior was not determined by the liquid film velocity affecting the behavior of the bubbles and vapor film [1] but by the amount of the liquid supplied to the WF. For a better understanding of the WF behavior, it needs to be confirmed which of the physical parameters are dominant. These physical factors are also considered to have significant effects on liquid film behavior on the chamber wall of the bipropellant thruster. In addition, from the viewpoint of the reduction in propellant consumption that leads to a higher performance of the bipropellant thruster and consequently a longer life of the satellite, the effect of the mass flow rate on the cooling processes needs to be examined further.

The flow rates in many previous studies on jet impingement cooling [1, 2, 3, 19, 26] were relatively high ($\sim O(1\text{-}100)$ L/min) because a large amount of water is used in material processes and cooling of nuclear reactor cores. On the other hand, results for the film formation processes under the condition of very low flow rate (< 7.0 g/s) have not been well reported [27], even though the optimization of the liquid for the film cooling is of importance [28]. Additionally, in many previous studies [1, 2, 3, 19], the liquid jet has been injected vertically onto the hot surface with a uniform temperature distribution, while the liquid is actually injected obliquely onto the wall with a spatial temperature gradient during the pulse firing mode in the actual thruster. Therefore, it is not certain whether the experimental findings of the previous studies can be observed during such quenching processes. The objectives of the present study are to evaluate whether the effect of the mass flow rate and the liquid jet velocity are dominant to the WF behavior and to investigate the heat transfer characteristics during oblique jet impingement quenching with a small amount of the test liquid in the case of the initial temperature distribution with a spatial gradient.

2. Experimental description

2.1 Experimental apparatus

Figure 2 shows a schematic illustration of the experimental apparatus used in the present study. While the liquid films injected from multiple injector holes may interfere with each other in the actual thruster, the quenching processes of a liquid film formed by a liquid jet were considered as the first step for understanding the cooling mechanism in the liquid film cooling. In this study, the impingement point of the liquid jet was defined as the origin. The $x, y,$ and z axes represent the direction of the liquid film flow, liquid film width, and perpendicular to the wall, respectively. The experimental apparatus consists of an injector part with a single nozzle, a metal plate (aluminum alloy (A5052), 3-mm thick, 50-mm wide, and 118-mm long), a liquid supply system, a high-speed camera, and an infrared camera. A rod heater was placed in the metal component on one side of the metal plate, as shown in Fig. 2, and the plate was heated to form a spatial temperature gradient in the x direction. The behavior of the liquid film formed on the heated plate was observed from the front (as shown in Fig.2) and the side simultaneously by using two high-speed cameras (Photron FASTCAM SA-1.1 and Vision Research Phantom v2012). The frame rate and exposure time were 500 fps and 20 μs. The spatial resolution for the front view and the side view were 0.14 and 0.09 mm/pixel, respectively. In addition, the temperature distribution of the test plate was measured from the backside using an infrared camera (NIPPON AVIONICS InfReC R550Pro). The backside of the test plate was coated with black body paint, ensuring an emissivity of 0.94. The frame rate for IR imaging was 60 fps with a spatial resolution of 0.23 mm/pixel. The measurement area for temperature of the test plate was limited to 60 mm downstream from the impingement point owing to the metal component with the rod heater, as shown in Fig. 2.

Water was selected as the test liquid because the density and surface tension of water were similar to those of hydrazine. To investigate the effect of the mass flow rate on the quenching processes, two nozzles with the diameters of 0.7 mm and 1.1 mm were used and the mass flow rate of water was varied from 3.0 g/s to 6.0 g/s in the increment of 1.0 g/s. The ratio of the distance from the nozzle tip to the test plate to the nozzle diameter L/d was set to 6. Although the impingement angle influences the formation of liquid film [7, 24, 25], the impingement angle θ was selected as 10° to simulate the situation in the actual thruster. The test liquid at room temperature (approximately 20°C) was injected onto the test plate when the temperature of the impingement point was raised to 220°C. The experimental conditions are presented in Table 1. For each condition, the cooling tests were conducted five times.

2.2 Estimation of the temperature and heat flux of the surface cooled by liquid film

For the data acquisition of surface temperature and surface heat flux on the cooled surface (front surface), the inverse heat conduction problem should be solved because the value of the Biot number was higher than 0.1 and the temperature distribution in the thickness direction could not be negligible [29]. In the present study, a rectangular calculation domain with a length of 70 mm, a width of 50 mm (measurement area) and a thickness of 3 mm consisted of 105×75×30 cells. The time step was dependent on the frame rate of the infra-red imaging and 1/60 s. Fujimoto et al. [30] conducted the three-dimensional steady-state inverse heat conduction analysis to estimate the surface heat flux and temperature distribution on the cooled surface of the test plate during the jet impingement cooling of the moving plate by using the measured temperature profile of the rear surface of the test plate. In [30], the authors applied the finite volume method. Recently, Haramura [31] proposed the robustly stable and easily usable scheme for solving the inverse problem of one-dimensional transient heat conduction with the fully implicit scheme, in which the finite difference method was applied. In the present study, the three-dimensional inverse problem of the transient heat conduction was numerically solved by employing the finite volume method as the discretization method and extending the scheme proposed by Haramura [31] from the one-dimensional problem to the three-dimensional problem.

The transient heat conduction equation of the plate in the Cartesian coordinate as shown in the plate of Fig. 2 is given by Eq. (2).

$$\rho_{\mathrm{w}} c_{\mathrm{w}} \frac{\partial T_{\mathrm{w}}}{\partial t} = k_{\mathrm{w}} \left(\frac{\partial^2 T_{\mathrm{w}}}{\partial x^2} + \frac{\partial^2 T_{\mathrm{w}}}{\partial y^2} + \frac{\partial^2 T_{\mathrm{w}}}{\partial z^2} \right) \tag{2}$$

In the finite volume method [32], the discretization of Eq. (2) with the fully implicit scheme for a control volume P is described as Eq. (3). The neighbors of the control volumes are represented as *E*, *W*, *N*, *S*, *T*, and *B*, as shown in Fig. 3(a). Subscript of *e*, *w*, *n*, *s*, *t*, and *b* denote each of the faces of the control volumes.

$$a_P T_P = a_E T_E + a_W T_W + a_N T_N + a_S T_S + a_T T_T + a_B T_B + a_P^0 T_p^0 \tag{3}$$

Here, $a_E = \frac{k_{\mathrm{w}e} \Delta y \Delta z}{(\delta x)_e}$, $a_W = \frac{k_{\mathrm{w}w} \Delta y \Delta z}{(\delta x)_w}$, $a_N = \frac{k_{\mathrm{w}n} \Delta z \Delta x}{(\delta y)_n}$, $a_S = \frac{k_{\mathrm{w}s} \Delta z \Delta x}{(\delta y)_s}$, $a_T = \frac{k_{\mathrm{w}t} \Delta x \Delta y}{(\delta z)_t}$, $a_B = \frac{k_{\mathrm{w}b} \Delta x \Delta y}{(\delta z)_b}$,

$a_P^0 = \frac{\rho_{\mathrm{w}} c_{\mathrm{w}} \Delta x \Delta y \Delta z}{\Delta t}$, $a_P = a_E + a_W + a_N + a_S + a_T + a_B + a_P^0$

and T_P^0 is the temperature of P in the previous time step. The time step and grid sizes for x, y and z directions were represented as Δt and Δx, Δy, Δz, respectively. The distance between the cells were denoted by δx, δy, and δz in each direction. The front and rear surfaces of the tested plate are set to be the boundaries of the computational domain. Designating the control volumes of row 1 as shown in Fig. 3(b), the temperature of the control volumes in the upper row are calculated from Eq. (4) which is the rearranged form of Eq. (3).

$$T_T = \frac{1}{a_T}\left(a_P T_P - a_E T_E - a_W T_W - a_N T_N - a_S T_S - a_B T_B - a_P^0 T_P^0\right) \tag{4}$$

If the boundary condition of the rear surface is given, the temperature of the control volumes in row 1 can be obtained. Then, the temperature in row 2 are obtained by the discretized equation for the control volumes in row 1. Using these values and Eq. (4), the temperature for upper rows can be derived in order. The last nodes in row N+1 shown in Fig. 3(b) are the virtual points located outside of the plate, and the surface temperature and heat flux are determined from the temperature of the control volumes in rows N and N+1, thermal conductivity, and the distance between row N and row N+1.

When calculating the temperature and heat flux of the front surface, the initial condition should be given. Figure 4 shows the difference between the temperature at a certain point on the front surface measured by a K-type thermocouple which has an error of ±2.5°C under the measured temperature range and that on the rear surface measured by an infra-red camera, during the plate heating. Owing to the heat-resistance of the thermocouple, the range of the measured temperature was below the initial condition, and it was confirmed that there was a slight temperature difference between the front surface and rear surface before the cooling. However, the difference between the two surfaces was within the tolerance of the thermocouple. Therefore, the temperature distribution in the thickness direction of the plate at t = 0 s was assumed to be uniform and the temperature profile of the rear surface was given as the initial condition. For the boundary conditions of the surfaces, zero temperature gradient conditions were given at the side boundaries in the y direction and the rear surface. The upstream side boundary in the x direction was also zero temperature gradient condition, and the downstream side boundary in the x direction was given by the heat flux determined by the thermal conductivity of the plate and the temperature gradient in the x direction at t = 0 s. In the present study, the metal properties of the aluminum alloy (A5052) were assumed to be constant (ρ_{w} = 2680 kg/m^3, c_{w} = 900 J/ kg K, and k_{w} = 137 W/m K).

In this method, the noises superposed on the temperature measurement have quite severe effects on determining the surface temperature and heat flux [30, 31]. Therefore, smoothing operations needed to be performed for the spatial directions and temporal direction before the calculation. The smoothing methods used for the spatial directions and temporal direction in the present study were cubic smoothing splines and the Savitzky-Golay method [33], which were also used in [30] and [31] respectively. The smoothing procedure was as follows: first, a smoothing operation using cubic smoothing splines was performed on the temperature profile data at each time by using a Python package CSAPS [34], and then the Savitzky-Golay method [33] was applied to the change of the temperature at each point.

3. Results and discussion

3.1 Wetting front propagation

Figure 5 (a) and (b) show the progress of the liquid film and the WF position on the x-axis as measured from the images under the condition of $\dot{m}$=5.0 g/s and d=0.7 mm. As explained later, the red solid line in Fig. 5 (b) indicates the fitting result of the WF position obtained by using Eq. (1). It can be observed in Fig. 5 that the liquid film expanded in the y direction and the WF moved downstream with the elapsed time since the cooling commenced. In addition, the velocity of the WF slowed down as the WF moved downstream, and this trend was also observed in the previous studies on quenching of the hot surface with vertical jet impinging [15, 18, 20, 26].

Figure 6 shows the direct image of the liquid film and the distributions of the estimated surface temperature and heat flux at t = 0.6 s after the cooling commenced. The maximum heat flux position lay in the wetted region near the WF as observed in [1, 3, 19] and the WF and maximum heat flux position were quite close [35]. In addition, the WF was located in the region where the spatial temperature gradient in the direction of the liquid film flow was the largest. Figure 7 shows the relationship between the position where the temperature gradient along the x direction achieved its maximum value x_{g} and the WF position x_{wf} under the condition of d = 0.7 mm and $\dot{m}$ = 5.0 g/s. These positions were consistent at any location from the impingement point; this agrees with the observations of Karwa and Stephan [19]. From the viewpoint of film cooling in an actual thruster which is difficult to visualize, this suggests that the length of the liquid film can be estimated from the distribution of the wall temperature observed in an actual thruster [12].

The effects of the liquid jet velocity and mass flow rate on the WF propagation were evaluated by varying the nozzle diameter under each mass flow rate condition. Figure 8 shows the time taken for WF to reach each position (x = 10, 20, 30, 40, and 50 mm) on the x-axis. The plots indicate the mean values of the five tests, and the error bars show the maximum and minimum values in the five tests. The time required for the WF to reach certain positions increased further downstream under all the experimental conditions, which meant that the WF velocity decreased as the WF moved downstream as seen in Fig. 5. Although the WF reached the position of x = 50 mm faster for the nozzle diameter of 0.7 mm under the conditions of $\dot{m}$ = 3.0 and 4.0 g/s, the time required for the WF to reach each position was almost the same under the same mass flow rate conditions. It can also be seen from Fig. 8 that regardless of the nozzle diameter the WF moved downstream faster with an increase in the mass flow rate. The liquid jet velocity increased by approximately 2.5 times when the nozzle was changed from 1.1 mm to 0.7 mm, and it led to the difference in the liquid film velocity. However, the effect of the mass flow rate appeared to be greater than that of the liquid jet velocity in the range of the experimental conditions used in this study (see Fig. 8), which corresponded to the results under the higher flow rate conditions [26]. Figure 9 shows the mean velocity of the liquid film and the film mass flow rate per unit liquid film width on the x axis under the condition of $\dot{m}$ = 5.0 g/s, which Inamura et al. [24] theoretically predicted for the liquid film formed by an oblique jet impinging on the non-heated wall. The mean liquid film velocity for d = 0.7 mm was higher at any position than that for d = 1.1 mm, while the film mass flow rate per unit liquid film width was almost the same for both; it was suggested that the mass flow rate, that is, the amount of the liquid supplied to the WF, was highly significant to the reduction of the plate temperature at the WF, leading to the faster movement of the WF with the increase of the mass flow rate.

Here, let us recall the possible reasons why the WF velocity decreased further downstream as suggested by Karwa et al. [15] and indicated in section 1. As mentioned above, the liquid film velocity may have negligible effects on the WF propagation. Therefore, the latter reason of Karwa et al. [15], i.e., the degree of heat the liquid film receives from the plate between the impingement point and the WF, may explain the deceleration of the WF propagation; the effect of the thermal boundary layer on the propagation of the WF was considered to be significant, compared with the effect of liquid film velocity. When the WF was located relatively close to the impingement point, the thickness of the thermal boundary layer in the liquid film was thin, and the bubbles condensed immediately after the initiation of growth, owing to subcooling. Furthermore, the thermal boundary layer of the liquid film at the WF thickened as the WF moved downstream, and it might have led to the growth of bigger bubbles and the prevention of WF propagation.

In the previous studies, the WF position was often expressed using Eq. (1). In the present study, the WF position on the x-axis was well-fitted by Eq. (1), as shown in Fig. 5. Figure 10 shows the effects of the mass flow rate and liquid jet velocity on the constant a and exponent n. As shown in Fig. 10(a), the value of constant a increases linearly with an increase in the mass flow rate, implying that the value of constant a was independent of the liquid jet velocity. These results agreed with the results reported in [18] because the increase in the liquid jet velocity corresponded to an increase in the liquid mass flow rate under the condition of a fixed nozzle diameter. It was also found in Fig. 10(b) that the value of the exponent n decreased slightly with the mass flow rate under the condition of d = 0.7 mm, while it remained almost constant under the condition of d = 1.1 mm. Furthermore, the value of exponent n for d = 0.7 mm is slightly higher than that for d = 1.1 mm, under the same mass flow rate conditions. The values were in the range of approximately 0.4–0.5, close to the values reported in [18] and [20]. For a constant a and exponent n, the same tendency as that in the previous studies on quenching with vertical jet impingement was observed in this study, where the liquid jet was obliquely injected onto the plate with a spatial temperature gradient.

3.2 Heat transfer characteristics during quenching process

Figure 11 shows the time history of the temperature for the front and rear side at each position on the x-axis under the condition of $\dot{m}$ = 5.0 g/s and d = 0.7 mm. The solid lines and broken lines indicate the front and rear surface temperature, respectively. The black dots indicate the temperature of the front surface when the WF reached each position. The front surface temperature dropped steeply compared to the rear surface temperature. The surface temperature at the instant WF position reached the measurement point took a constant value of approximately 200 °C up to around x = 20 mm. That temperature decreased as the WF moved downstream. The temperature decreased from its initial value before the arrival of the WF further downstream. This is due to the conduction of heat by the plate, between the wetted regions and dry regions. The area that exhibits temperature decrease, despite not being wetted by the liquid film, is termed as the precursory cooling zone (PCZ) [36]. Figure 12 shows the value of the Peclet number as defined in Eq. (5) [37, 38] at each position.

$$Pe = \frac{u_{\mathrm{wf}}\delta}{\alpha_{\mathrm{w}}}. \tag{5}$$

u_{wf} and α_{w} indicate the WF velocity and thermal diffusivity of the test plate, respectively. In the present study, the WF velocity at each position (x = 10, 20, 30, 40, and 50 mm) was calculated as the ratio of the distance between each position (10 mm) to the time taken to travel from one position to another. As shown in Fig. 12, the value of the Peclet number decreased in the downstream. This means that the effect of the thermal diffusion rate gradually increased, and it adequately accounted for the prominent precursory cooling effect by the heat conduction through the plate, in the downstream, as shown in Fig. 11.

Figure 13 shows the time history of the surface heat flux, at each position under the condition of $\dot{m}$ = 5.0 g/s and d = 0.7 mm, for evaluating the heat transfer characteristics between the liquid film and the test plate. The maximum heat flux at each position was achieved after the WF passed, as discussed in section 3.1. Subsequently, the cooling mode gradually shifted from the nucleate boiling to the single-phase forced convection. As shown in Fig. 13, the value of the maximum heat flux achieved at each position decreased with an increase in the distance from the impingement point. This tendency was reported in the previous studies on the quenching of hot surfaces with vertical jet impingement [3, 19]. Figure 14 shows the boiling curves at each position on the x-axis under the condition of $\dot{m}$ = 5.0 g/s for d = 0.7 and 1.1 mm. ΔT_{sup} denotes the degree of wall superheat which means the difference between the plate (wall) surface temperature and the saturated temperature of the test liquid. The peak value of the heat flux decreased further downstream as shown in Fig. 13, although the degree of wall superheat at the maximum heat flux point was nearly constant. Comparing Fig. 14(a) and (b), the heat flux for d = 0.7 mm in the single-phase convection regime was higher than that for d = 1.1 mm because the liquid film velocity for d = 0.7 mm was higher than that for d = 1.1 mm as shown in Fig. 9, while the values of the maximum heat flux in the nucleate boiling regime were similar at each position, although the liquid jet velocity was approximately 2.5 times different.

Figure 15 shows the change in the maximum heat flux q_{max} with the distance from the impingement point. The value of the maximum heat flux decreased with the distance from the impingement point under all conditions because the liquid was warmer further downstream from the impingement point. In addition, the maximum heat flux increased with an increase in the mass flow rate because the increase of the liquid temperature was smaller due to the higher heat capacity of the liquid film. From these results, it could be suggested that the WF propagation speed was determined by the heat removal rate near the WF, leading to the temperature drop, and the effect of the mass flow rate on it was higher than that of the jet velocity, as discussed in section 3.1.

3.3 Amount of heat removal from plate to liquid film and evaporative fraction

In the present study, the temperature profile in the xy plane was measured, and the distribution of the surface heat flux in the xy plane could be estimated by inverse heat conduction analysis. Using the values of the estimated surface heat flux in the xy-plane, the amount of heat removal from the plate to the liquid film and the evaporative fraction of the liquid film were estimated to evaluate the mass fraction of the injected liquid that contributed to the cooling of the test plate. Figure 16 shows the liquid film and the surface heat flux distribution at t = 0.6 s under the condition of $\dot{m}$ = 5.0 g/s and d = 0.7 mm. The amount of heat removal from the plate to the test liquid $\dot{Q}$ was calculated for the area where the value of the estimated surface heat flux was positive according to the following equation.

$$\dot{Q} = \iint q_s dxdy. \quad (6)$$

Figure 17 shows the amount of the heat removal at the elapsed time when the WF reached close to x = 30 mm under each mass flow rate condition; $\dot{Q}$ of $\dot{m}$ = 3.0, 4.0, 5.0, and 6.0 g/s corresponded to the value at t = 1.2, 0.8, 0.6, and 0.4 s, respectively (see Fig. 5). The liquid film removed more heat from the test plate as the mass flow rate increased for each nozzle diameter because the maximum heat flux assumed a higher value with an increase in the mass flow rate, as shown in Fig. 15. An additional reason was that the wetted area increased with an increase of the mass flow rate [7]. Comparing the values under the same mass flow rate conditions, the smaller the nozzle diameter, the higher was the amount of the heat removal because the maximum heat flux was slightly higher for smaller diameters. In addition, heat removal by single-phase forced convection was greater for the smaller diameter owing to the higher velocity of the liquid film as shown in Fig. 14.

Next, the mass fraction of the injected liquid that contributed to the cooling of the test plate was evaluated. To evaluate the fraction, the evaporative fraction $\emptyset$ defined in Eq. (7) was used.

$$\emptyset = \frac{\dot{Q}}{\dot{m} h_{\mathrm{lv}}}. \quad (7)$$

h_{lv} denotes the latent heat of the test liquid. Figure 18 shows the evaporative fraction calculated using Eq. (7) for the results shown in Fig. 17. The fraction of the injected liquid contributing to the cooling of the plate was nearly 10 % in the case of d = 0.7 mm and 8 % in the case of d = 1.1 mm (possibly overestimated due to effect of neglecting the sensible heat) and was almost the same under each mass flow rate condition, while the amount of the heat removal increased with an increase in the mass flow rate. Figure 18 suggests that nearly 90 % or more of the injected liquid was splashed away from the WF without evaporation.

4. Conclusions

An experimental study on the jet impingement cooling of a heated wall with a spatial temperature gradient was conducted to investigate the effect of the mass flow rate and the liquid jet velocity on the cooling processes, using a liquid film with an oblique impingement jet, by varying the nozzle diameter. Water and aluminum alloy were used as the test liquid and plate, respectively. The behavior of the liquid film on the heated wall was visualized using high-speed imaging. In addition, the temperature distribution of the surface opposite the cooling surface was obtained using infrared images to estimate the surface temperature and heat flux of the cooled side by solving the inverse problem of three-dimensional transient heat conduction.

The WF gradually moved downstream, and the velocity of the WF decreased as it moved downstream. It was notable that the WF propagation was affected by the liquid mass flow rate and not by the liquid jet velocity being related to the liquid film velocity even though, in this study, the velocity of the liquid jet was approximately 2.5 times different, and the WF moved faster as the mass flow rate increased. The WF position was well-fitted by a power function of elapsed time, and the constant had a linear relationship with the mass flow rate, while the exponent was in the range of approximately 0.4–0.5 which agreed with the results reported in the previous studies on quenching, with a vertical impingement jet.

The heat transfer characteristics during the quenching process were examined. The temperature at the relatively upstream location dropped immediately after the WF reached the respective position, while the temperature at the positions further downstream decreased before the arrival of the WF because of the effect of the precursory cooling induced by the solid heat conduction between the wetted and dry regions. The maximum heat flux decreased as the WF moved downstream, and the attained value was almost the same under the same mass flow rate conditions for the same positions, although the nozzle diameter was changed and the velocity of the liquid jet and formed film was different.

The amount of the heat removal from the test plate to the liquid film was calculated, and the fraction of the injected liquid contributing to the cooling of the test plate was estimated. The amount of heat removal increased as the mass flow rate increased for each nozzle diameter, and it assumed a higher value upon using a nozzle with a smaller diameter. However, the evaporative fraction, which is defined as the ratio of the amount of heat removal to the product of the mass flow rate and the latent heat of the liquid, assumed almost the same value for each nozzle diameter and was nearly 10 % or less. These results suggest that nearly 90 % or more of the injected liquid was splashed away from the test plate without evaporation.

References

[1] B. Wang, D. Lin, Q. Xie, Z. Wang, and G. Wang, "Heat transfer characteristics during jet impingement on a high-temperature plate surface," *Appl. Therm. Eng.*, vol. 100, pp. 902–910, 2016.

[2] S. G. Lee, M. Kaviany, C. J. Kim, and J. Lee, "Quasi-steady front in quench subcooled-jet impingement boiling: Experiment and analysis," *Int. J. Heat Mass Transf.*, vol. 113, pp. 622–634, 2017.

[3] J. Hammad, Y. Mitsutake, and M. Monde, "Movement of maximum heat flux and wetting front during quenching of hot cylindrical block," *Int. J. Therm. Sci.*, vol. 43, no. 8 SPEC. ISS., pp. 743–752, 2004.

[4] A. K. Sharma, U. K. Lodhi, G. Kumar, and S. K. Sahu, "Effect of Jet Inclination and Coolant Flow Rate on Thermal and Rewetting Behavior during Bottom Jet Impingement on Hot Horizontal Surfaces," *Steel Res. Int.*, vol. 90, no. 10, pp. 1–17, 2019.

[5] T. Okawa, K. Yamagata, and Y. Umehara, "Measurement of heat transfer coefficient profile during quenching of a vertical hot wall with a falling liquid film," *Nucl. Eng. Des.*, vol. 363, Article 110629, 2020.

[6] G. Fujii, Y. Daimon, C. Inoue, D. Shiraiwa, N. Tanaka, and K. Furukawa, "Visualization of pulse firing mode in hypergolic bipropellant thruster," *J. Propuls. Power*, vol. 36, no. 5, pp. 671–684, 2020.

[7] N. Sako, J. Hayashi, Y. Daimon, H. Tani, and H. Kawanabe, "Experimental analysis of the

spreading of a liquid film on a bipropellant thruster chamber wall," *J.Therm.Sci.Technol.*, vol. 16, Issue 1, pages JTST0008, 2021.

[8] W. Webber and R. Hoffman, "A mechanistic model for analysis of pulse-mode engine operation," in *8th Joint Propulsion Specialist Conference*, AIAA-72-1184, 1972.

[9] S. Iihara, H. Miyajima, and R. Nagashima, "Hydrazine/NTO liquid apogee engine for the ETS-VI," in *23rd Joint Propulsion Conference*, 1987, AIAA-87-1936.

[10] Y. Matsuura and Y. Tashiro, "Hypergolic Propellant Ignition Phenomenon with Oxidizer Two-Phase Flow Injection," in *49th AIAA/ASME/SAE/ASEE Joint Propulsion Conference*, AIAA-2013-4154, 2013.

[11] H. Tani, Y. Daimon, M. Sasaki, and Y. Matsuura, "Atomization and hypergolic reactions of impinging streams of monomethylhydrazine and dinitrogen tetroxide," *Combust. Flame*, vol. 185, pp. 142–151, 2017.

[12] Y. Daimon, H. Negishi, H. Tani, Y. Matsuura, S. Iihara, and S. Takata, "Flow field and heat transfer analysis in a MON/MMH bipropellant rocket engine," *Int. J. Energ. Mater. Chem. Propuls.*, vol. 16, no. 3, pp. 263–280, 2017.

[13] S. Takata, Y. Daimon, K. Sugimori, N. Matsuda, and Y. Tashiro, "Design verification results of japanese 120N Bi-propellant thrusters (HBT-1) based on its first flight in HTV3," *49th AIAA/ASME/SAE/ASEE Joint Propulsion Conference*, AIAA-2013-3754, 2013.

[14] M. Monde, "Heat Transfer Characteristics during Quench of High Temperature Solid," *J. Therm. Sci. Technol.*, vol. 3, no. 2, pp. 292–308, 2008.

[15] N. Karwa, T. Gambaryan-Roisman, P. Stephan, and C. Tropea, "Experimental investigation of circular free-surface jet impingement quenching: Transient hydrodynamics and heat transfer," *Exp. Therm. Fluid Sci.*, vol. 35, no. 7, pp. 1435–1443, 2011.

[16] P. Fu, L. Hou, Z. Ren, Z. Zhang, X. Mao, and Y. Yu, "A droplet/wall impact model and simulation of a bipropellant rocket engine," *Aerosp. Sci. Technol.*, vol. 88, pp. 32–39, 2019.

[17] I. A. Mudawar, T. A. Incropera, and F. P. Incropera, "Boiling heat transfer and critical heat flux

in liquid films falling on vertically-mounted heat sources," *Int. J. Heat Mass Transf.*, vol. 30, no. 10, pp. 2083–2095, 1987.

[18] Y. Mitsutake and M. Monde, "Heat transfer during transient cooling of high temperature surface with an impinging jet," *Heat Mass Transf. und Stoffuebertragung*, vol. 37, no. 4–5, pp. 321–328, 2001.

[19] N. Karwa and P. Stephan, "Experimental investigation of free-surface jet impingement quenching process," *Int. J. Heat Mass Transf.*, vol. 64, pp. 1118–1126, 2013.

[20] N. Hatta, J. Kokado, K. Hanasaki, "Numerical Analysis of Cooling Characteristics for Water Bar," *Trans. Iron Steel Inst. Japan*, vol. 23, no. 7, pp. 555–564, 1983.

[21] Y. Liu, H. Nakai, Y. Mitsutake, and M. monde, "Experimental study on transient boiling heat transfer around wetting front during subcooled jet impingement quenching," *Thermal Science and Engineering*, vol. 29, no. 1. pp. 9–17, 2021.

[22] A. H. Nobari, V. Prodanovic, and M. Militzer, "Heat transfer of a stationary steel plate during water jet impingement cooling," *Int. J. Heat Mass Transf.*, vol. 101, pp. 1138–1150, 2016.

[23] R. K. Bhagat, N. K. Jha, P. F. Linden, and D. I. Wilson, "On the origin of the circular hydraulic jump in a thin liquid film," J. Fluid Mech., vol. 851, p. R5, 2018.

[24] T. Inamura, H. Yanaoka, and T. Tomoda, "Prediction of Mean Droplet Size of Sprays Issued from Wall Impingement Injector," *AIAA J.*, vol. 42, no. 3, pp. 614–621, 2004.

[25] R. K. Bhagat and D. I. Wilson, "Flow in the thin film created by a coherent turbulent water jet impinging on a vertical wall," *Chem. Eng. Sci.*, vol. 152, pp. 606–623, 2016.

[26] A. V. S. Oliveira et al., "Experimental study of the heat transfer of single-jet impingement cooling onto a large heated plate near industrial conditions," *Int. J. Heat Mass Transf.*, vol. 184, Article 121998, 2022.

[27] R. M. Good and W. K. Nollet, "Fluid film distribution investigation for liquid film cooling application," *53rd AIAA/ASME/SAE/ASEE Joint Propulsion Conference*, 2017.

[28] S. R. Shine and S. S. Nidhi, "Review on film cooling of liquid rocket engines," *Propuls. Power*

Res., vol. 7, no. 1, pp. 1–18, 2018.

[29] A. Bejan and A. D. Kraus, Heat transfer handbook, vol. 1. John Wiley & Sons, 2003.

[30] H. Fujimoto, K. Tatebe, Y. Shiramasa, T. Hama, and H. Takuda, "Heat Transfer Characteristics of a Circular Water Jet Impinging on a Moving Hot Solid," *ISIJ Int.*, vol. 54, no. 6, pp. 1338–1345, 2014.

[31] Y. Haramura, "Inverse Heat Conduction Solution Utilizing the Difference Method with an Exact Matching Rule," *Thermal science and engineering*, vol. 29, no. 2. pp. 33–43, 2021.

[32] S.V.Patankar, "Numerical heat transfer and fluid flow (1st ed.)," CRC Press, 1980.

[33] M. J. E. Savitzky, A.; Golay, "Smoothing and Differentiation of Data by Simplified Least Squares Procedures," *Anal. Chem*, vol. 36, no. 8, pp. 1627–1639, 1964.

[34] https://pypi.org/project/csaps/

[35] D. J. Butterfield, B. D. Iverson, D. Maynes, and J. Crockett, "Transient heat transfer of impinging jets on superheated wetting and non-wetting surfaces," *Int. J. Heat Mass Transf.*, vol. 175, Article 121056, 2021.

[36] C. Agrawal, "Surface Quenching by Jet Impingement − A Review," *Steel Res. Int.*, vol. 90, no. 1, pp. 1–22, 2019.

[37] C. L. Tien and L. S. Yao, "Analysis of Conduction-Controlled Rewetting of a Vertical Surface," *J. Heat Transfer*, vol. 97, no. 2, pp. 161–165, 1975.

[38] K. H. Sun, G. E. Dix, and C. L. Tien, "Effect of Precursory Cooling on Falling-Film Rewetting," *J. Heat Transfer*, vol. 97, no. 3, pp. 360–365, 1975.

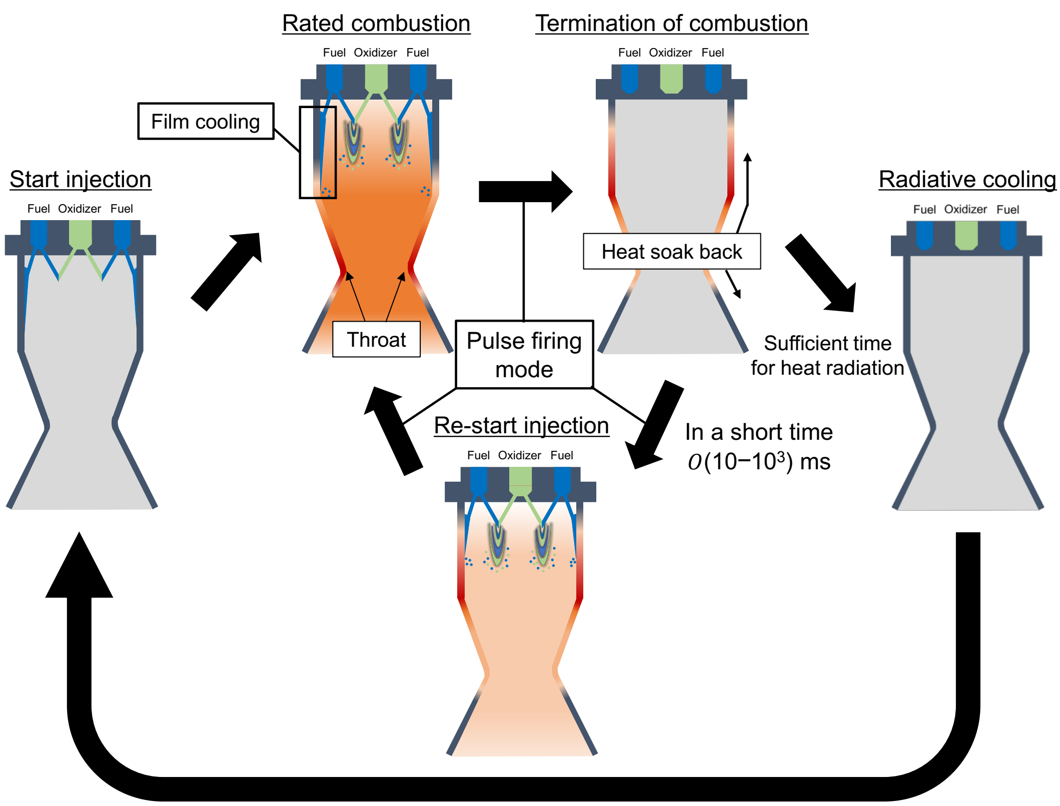

Fig. 1 Schematic of operation pattern of bipropellant thruster.

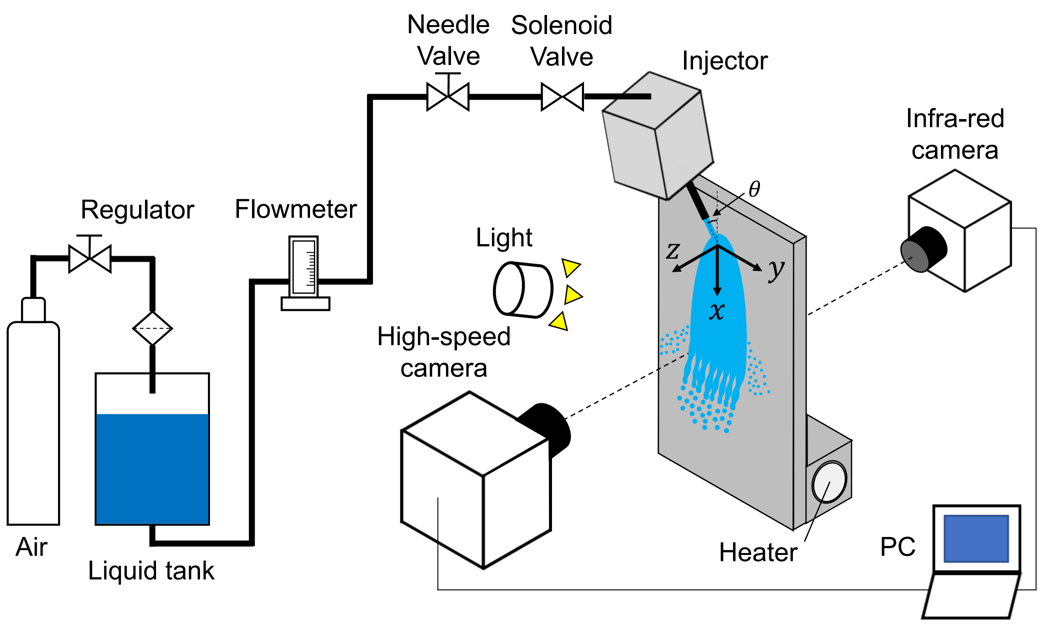

Fig. 2 Schematic of experimental apparatus.

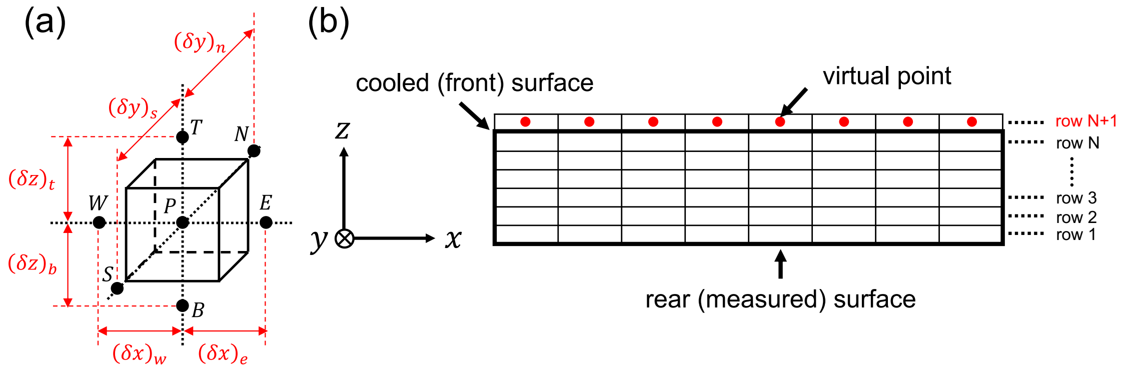

Fig. 3 Schematics of control volume ***P*** (a) and calculation domain (b).

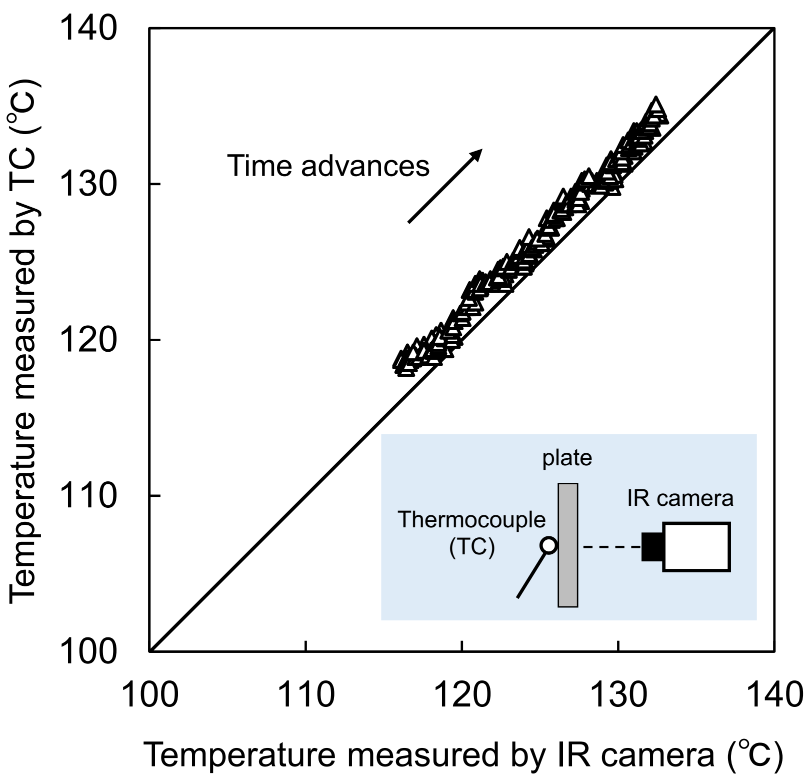

Fig. 4 Temperature difference between front surface and rear surface during plate heating.

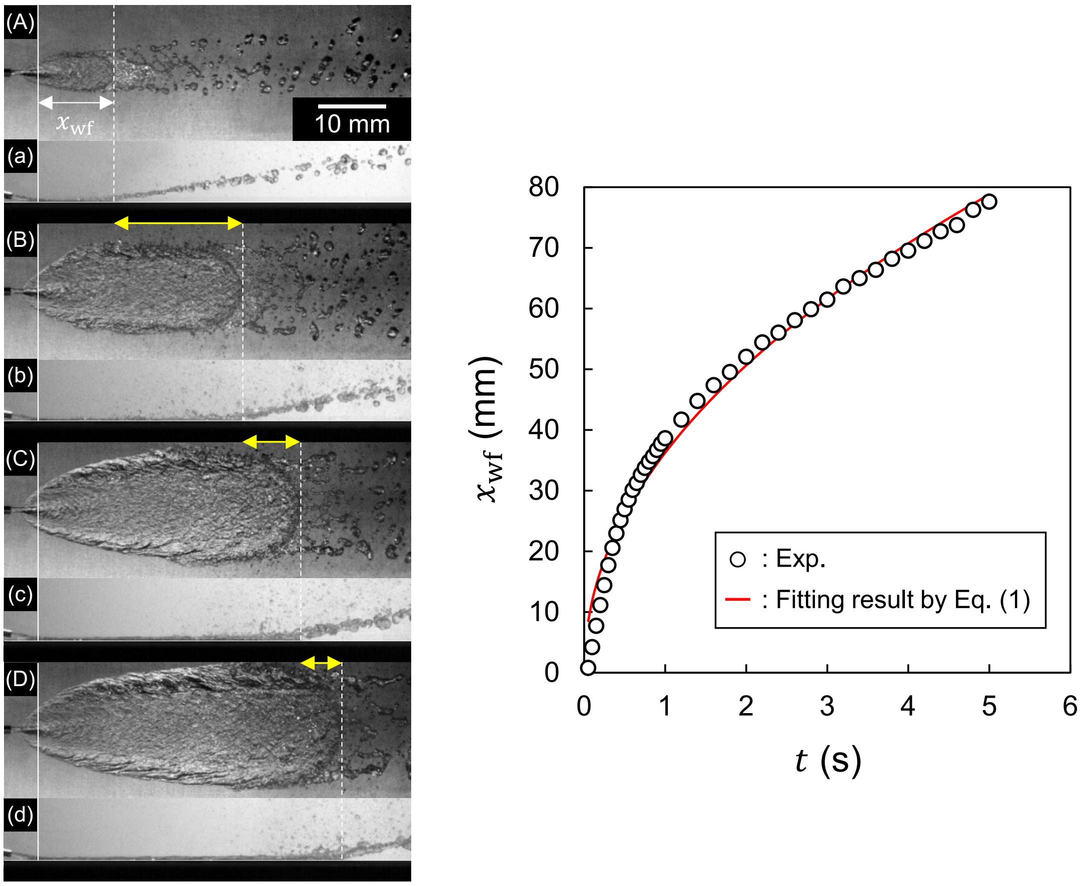

Fig. 5 Direct images of liquid film at each elapsed time under the condition of d = 0.7 mm and $\dot{m}$ = 5.0 g/s (left) and WF position with elapsed time (right). The images of the capital letters and the small letters respectively show the front views and the side views. (A, a): t = 0.2 s, (B, b): t = 0.6 s, (C, c): t = 1.0 s, (D, d): t = 1.4 s.

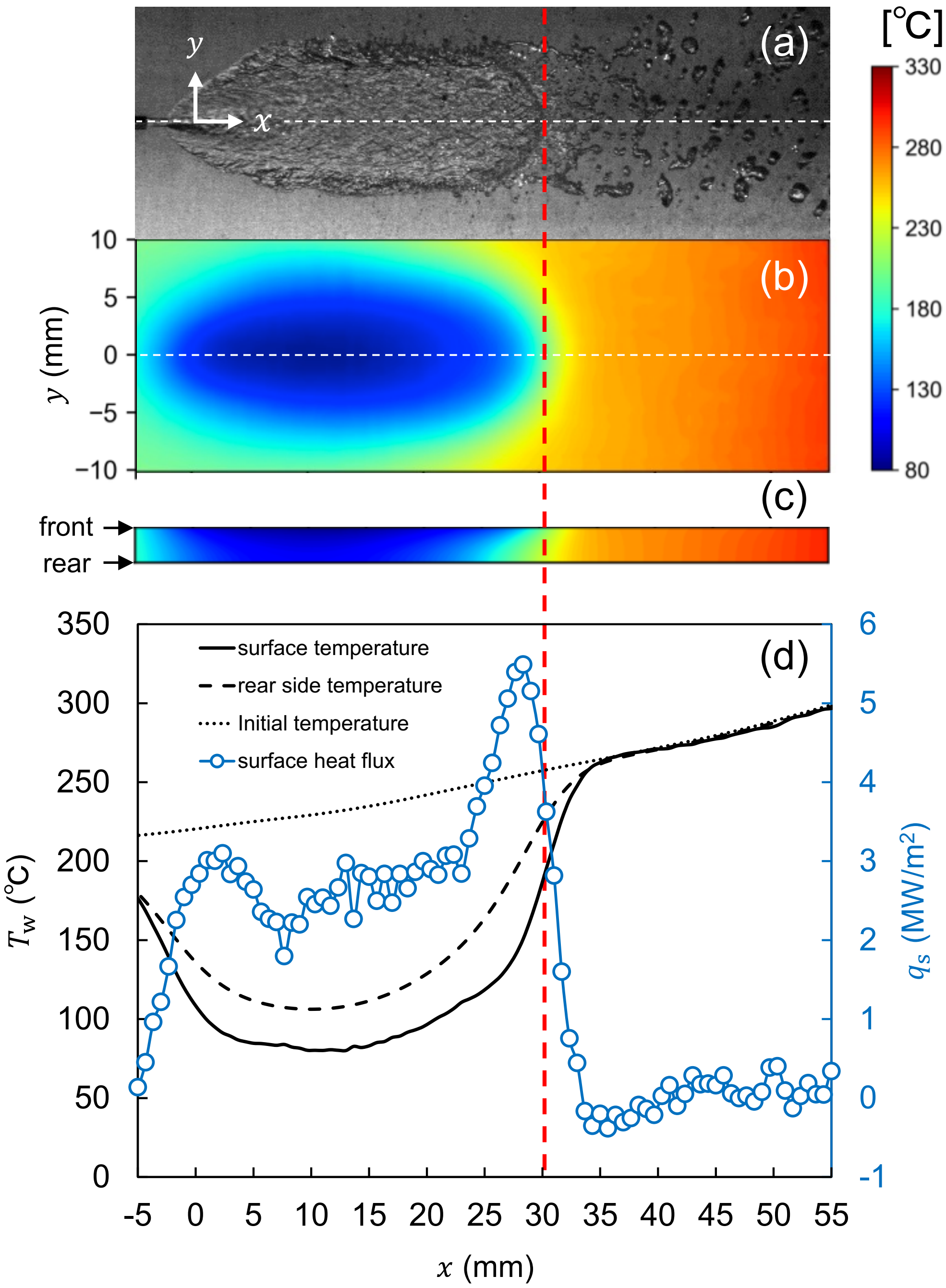

Fig. 6 Direct image of the liquid film (a), thermal images of temperature distribution of the front surface (b) and in the $\boldsymbol{xz}$-plane for $\boldsymbol{y}$ = 0 (c), and estimated surface temperature and heat flux distribution along the $\boldsymbol{x}$-axis for $\boldsymbol{y}$ = 0 calculated (d) at the elapsed time of 0.6 s. Red broken line indicates the WF position.

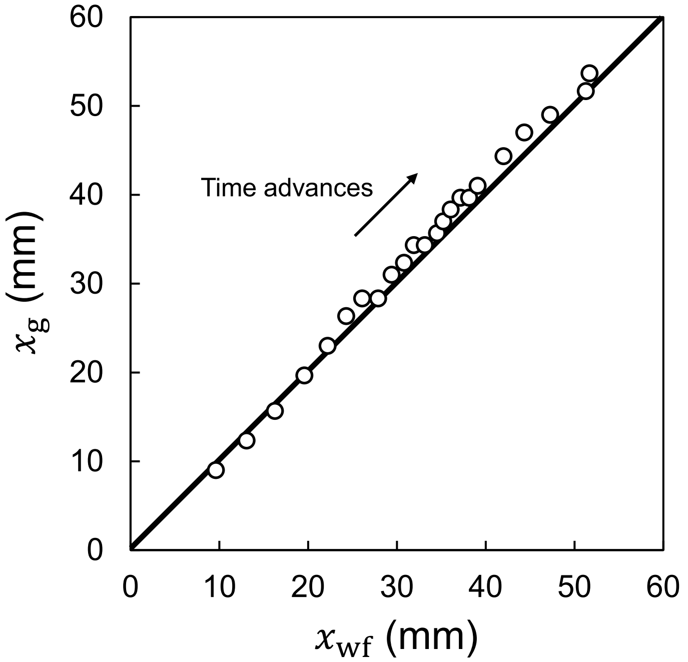

Fig. 7 Relationship between WF position and position where spatial temperature gradient takes its maximum value on the x-axis.

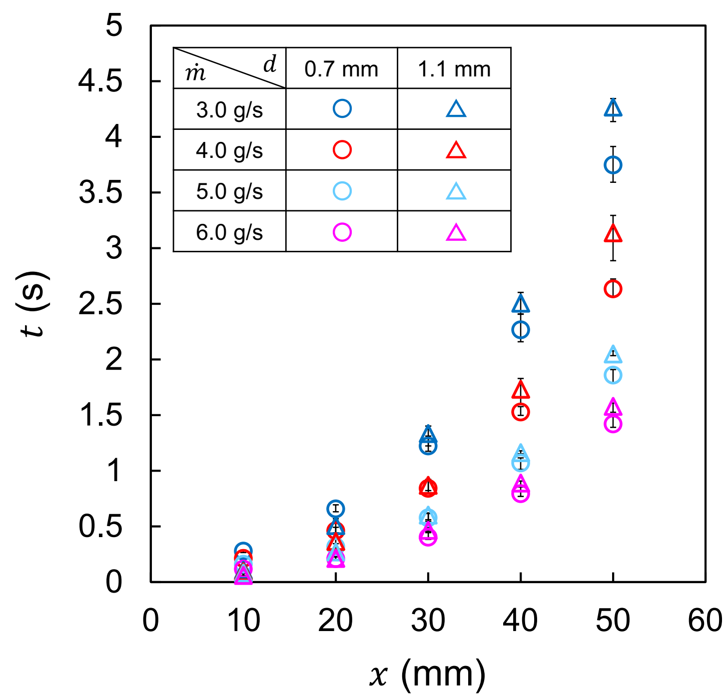

Fig. 8 Elapsed time when WF reaches certain positions on the x-axis.

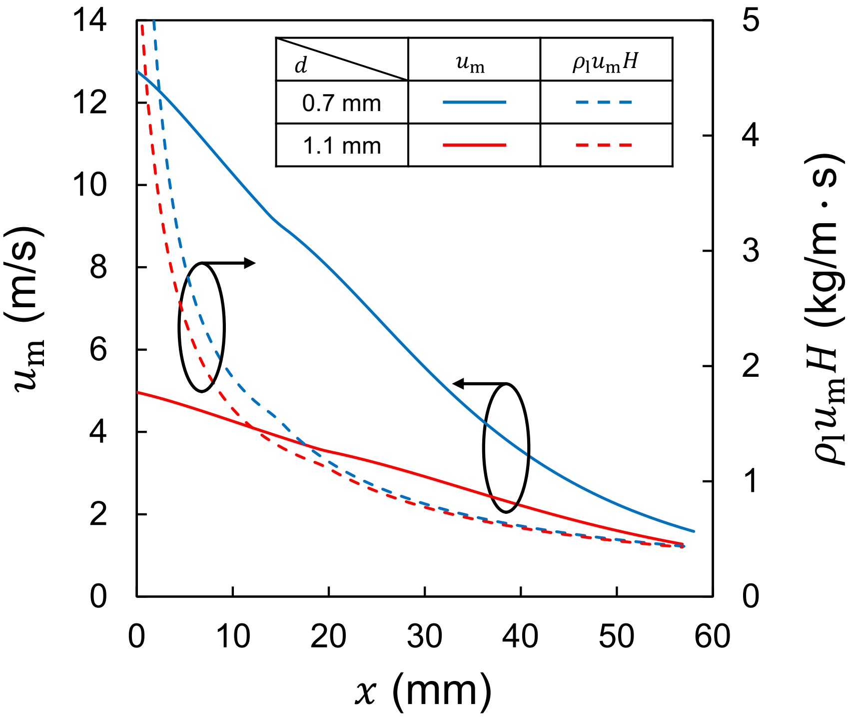

Fig. 9 Mean velocity of liquid film and film mass flow rate per unit liquid film width on the x axis under the condition of $\dot{m}$ = 5.0 g/s predicted by the model in [24].

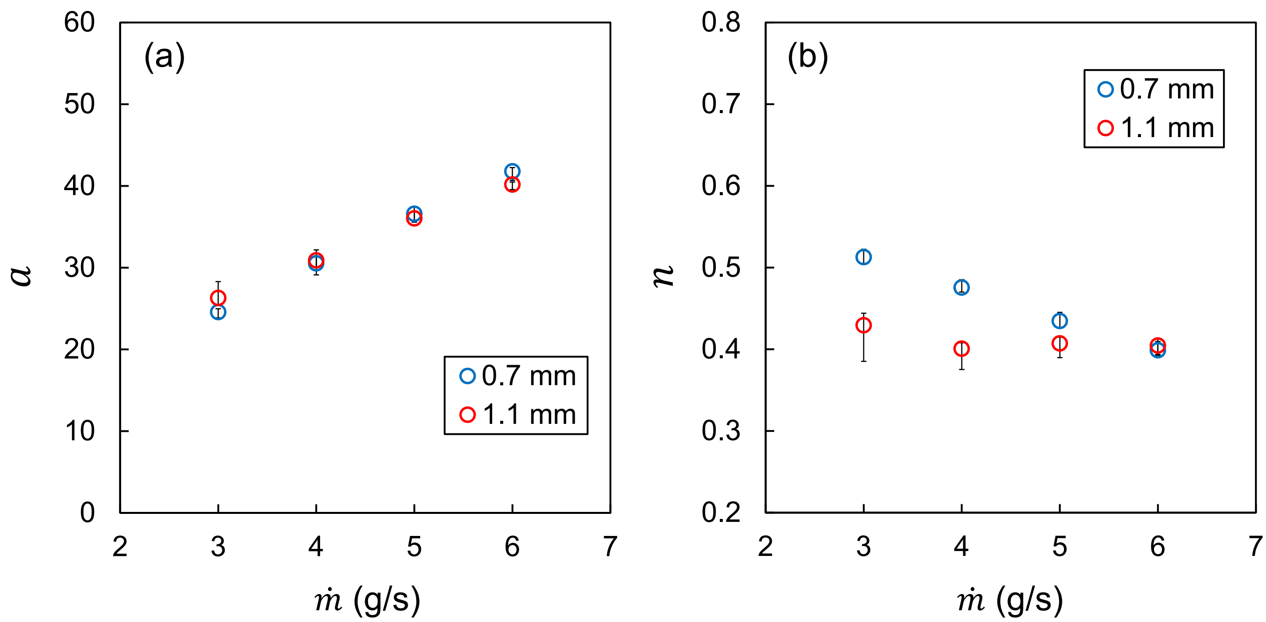

Fig. 10 Effects of mass flow rate and jet velocity on constant $\boldsymbol{a}$ (a) and exponent $\boldsymbol{n}$ (b).

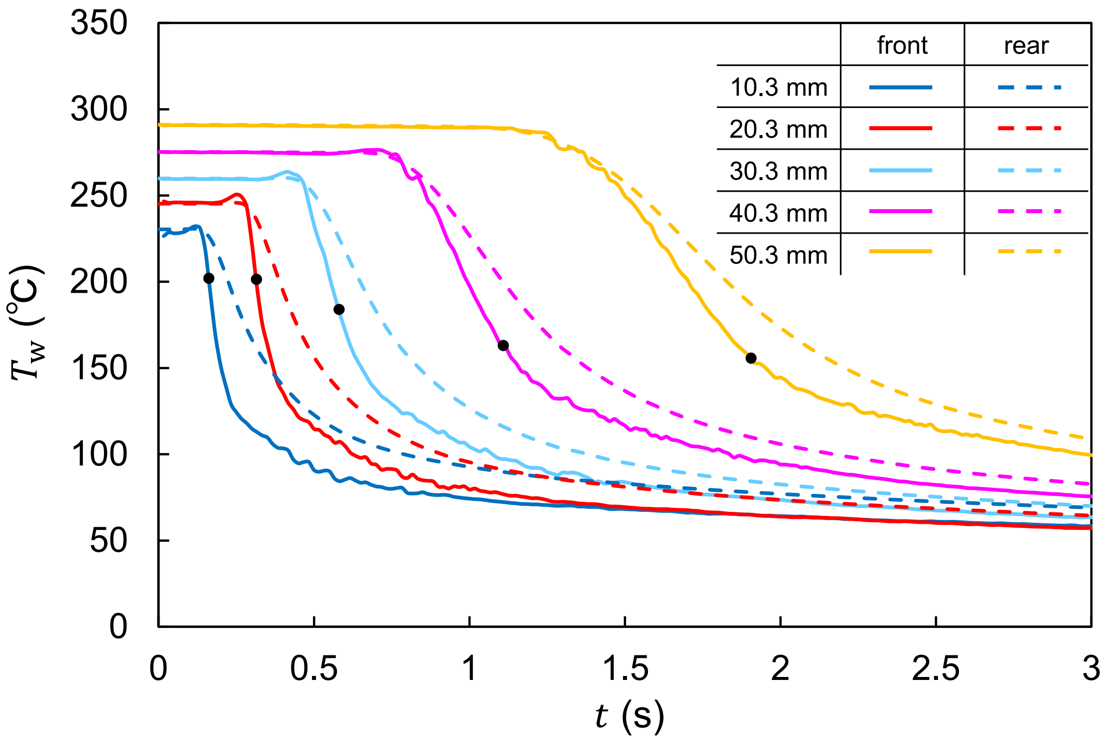

Fig. 11 Temperature history at each position on the $\boldsymbol{x}$-axis under the condition of $\boldsymbol{d}$ = 0.7 mm and $\dot{\boldsymbol{m}}$ = 5.0 g/s. The black dots indicate the temperature at the moment when the WF reached each position.

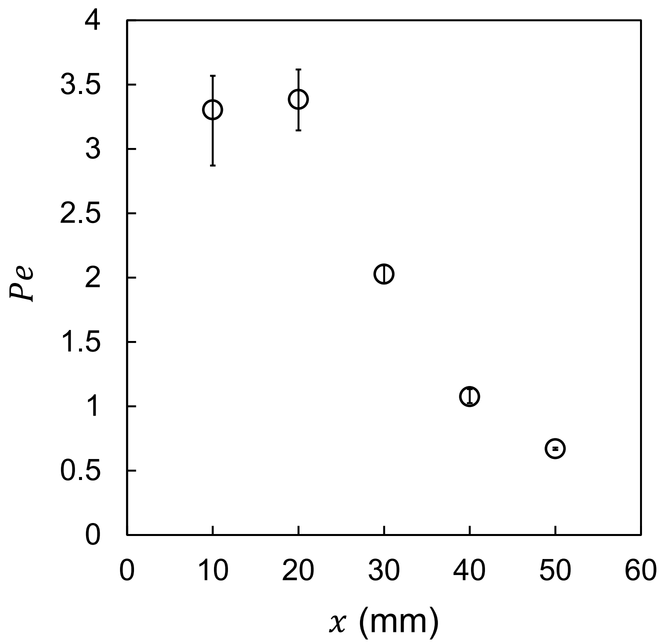

Fig. 12 Change in Peclet number under the condition of $\boldsymbol{d}$ = 0.7 mm and $\dot{\boldsymbol{m}}$ = 5.0 g/s.

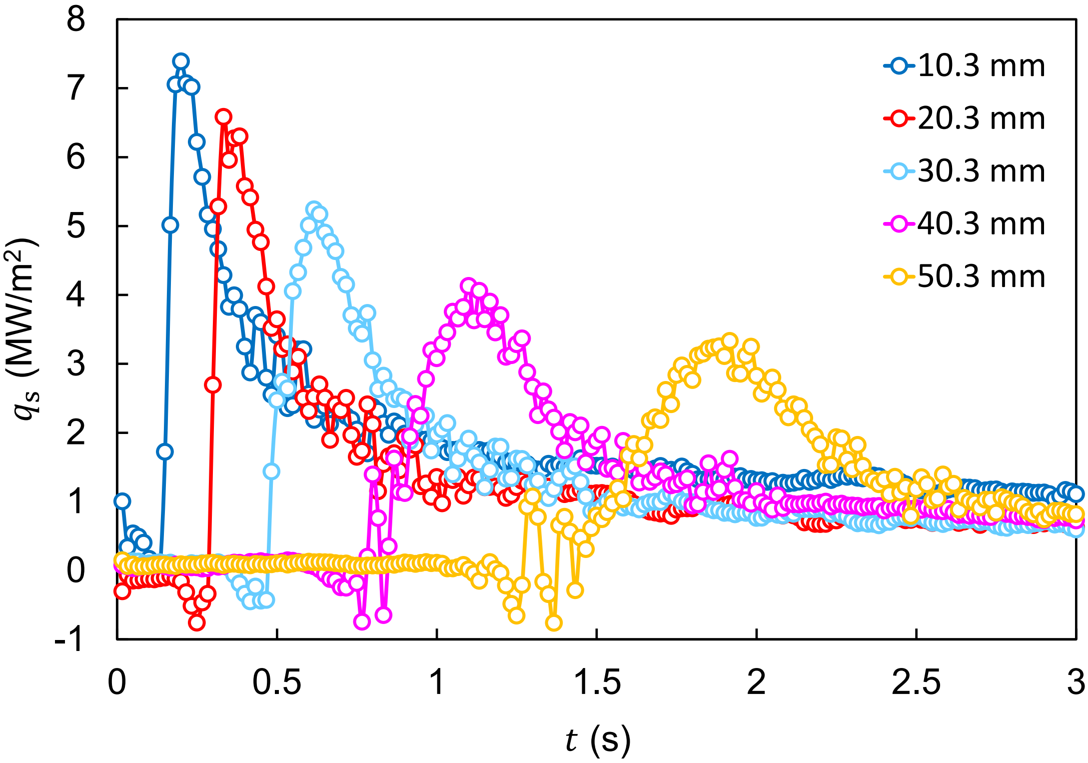

Fig. 13 Time history of heat flux at each position on the $\boldsymbol{x}$-axis under the condition of $\boldsymbol{d}$ = 0.7 mm and $\dot{\boldsymbol{m}}$ = 5.0 g/s.

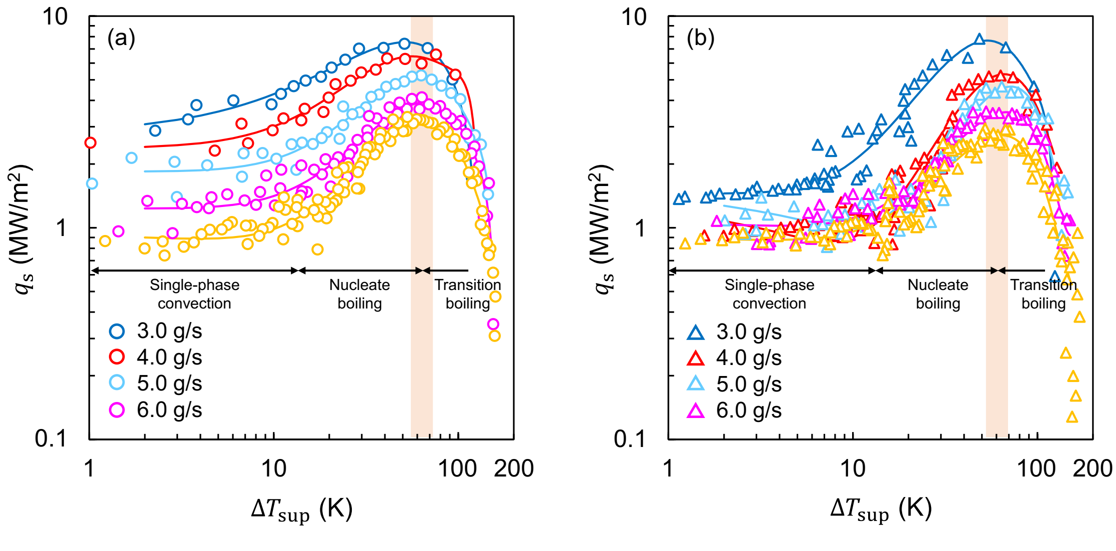

Fig. 14 Boiling curves at each position on the $\boldsymbol{x}$-axis under the condition of $\boldsymbol{d}$ = 0.7 mm (a) and $\boldsymbol{d}$ = 1.1 mm (b) for $\dot{\boldsymbol{m}}$ = 5.0 g/s.

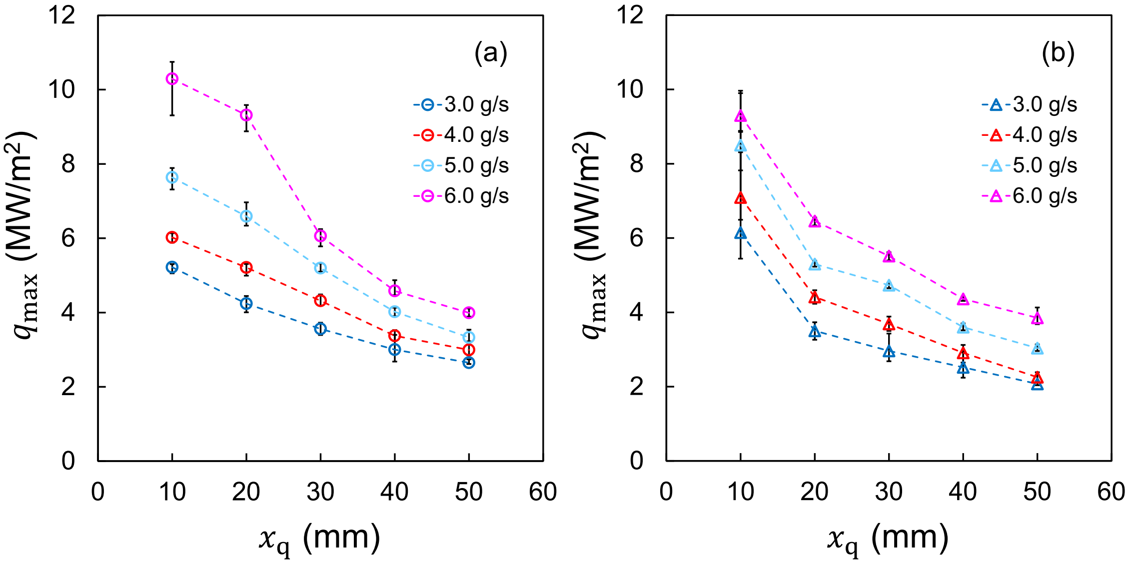

Fig. 15 History of maximum heat flux at each position on the $\boldsymbol{x}$-axis under the condition of $\boldsymbol{d}$ = 0.7 mm (a) and $\boldsymbol{d}$ = 1.1 mm (b).

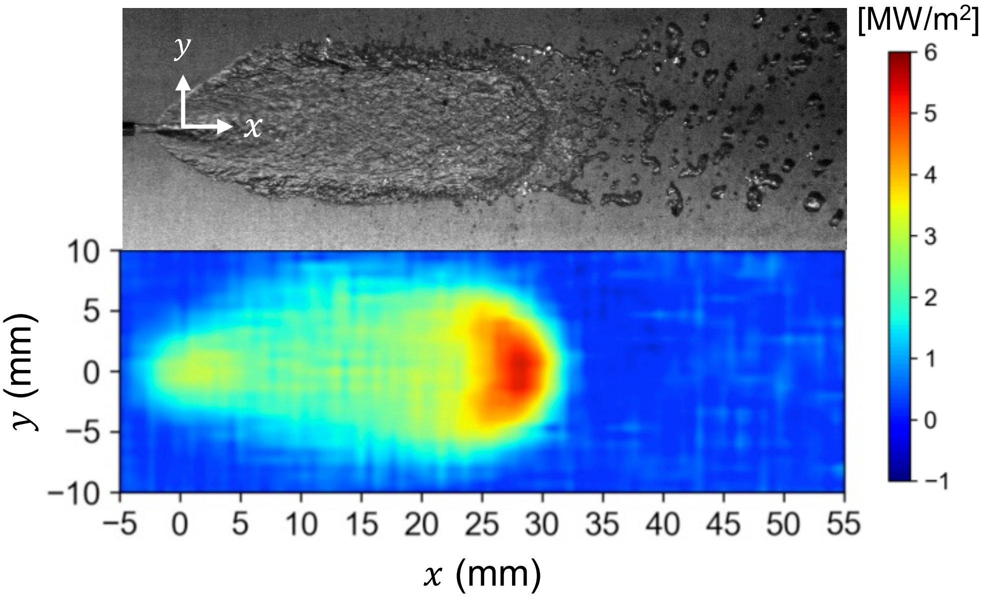

Fig. 16 Direct image of liquid film and distribution of heat flux at $\boldsymbol{t}$ = 0.6 s under the condition of $\boldsymbol{d}$ = 0.7 mm and $\dot{\boldsymbol{m}}$ = 5.0 g/s.

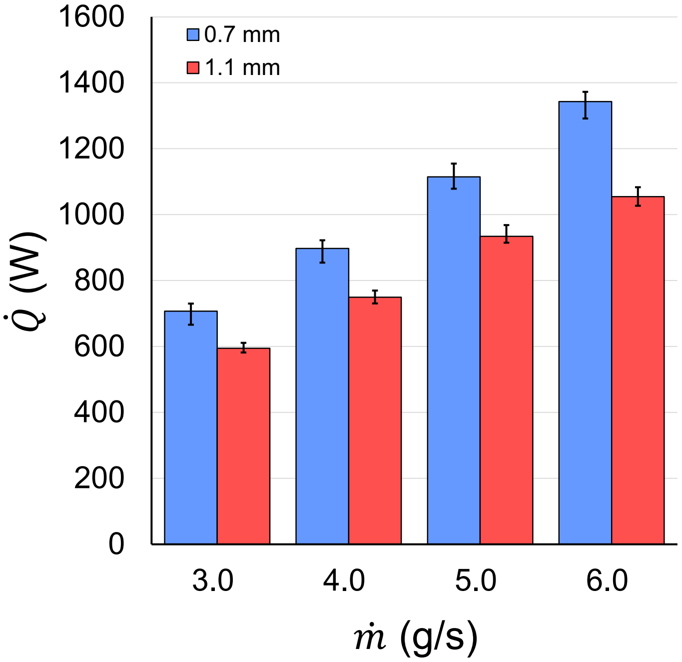

Fig. 17 Amount of heat removal from test plate to liquid film at elapsed time when the WF reached close to $\boldsymbol{x}$ = 30 mm.

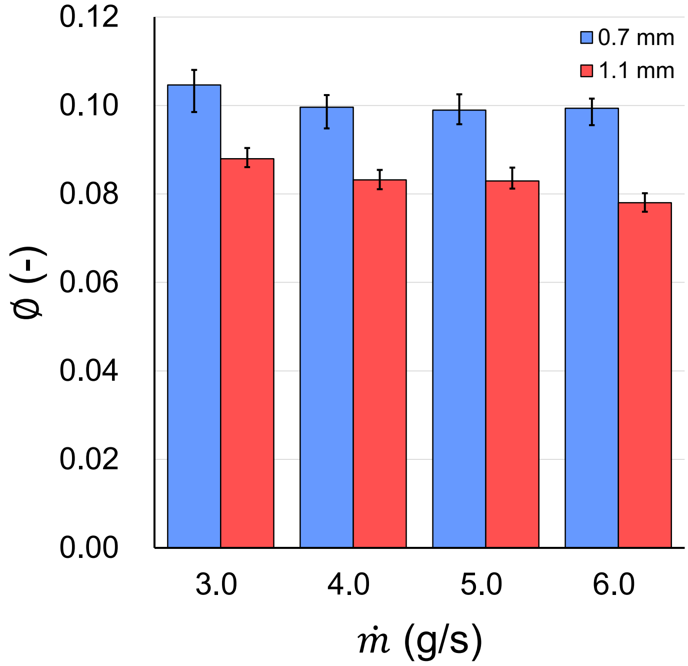

Fig. 18 Evaporative fractions at elapsed time when the WF reached close to $\boldsymbol{x}$ = 31 mm.

Table 1 Experimental conditions

Mass flow rate of test liquid	[g/s]	3.0, 4.0, 5.0, 6.0
Nozzle diameter	[mm]	0.7, 1.1
Jet Reynolds number	[-]	5400, 7200, 9100, 10900 (d = 0.7 mm)
		3500, 4600, 5800, 6900 (d = 1.1 mm)
Impingement angle	[°]	10
Degree of subcooling	[K]	80